iScience

Article

Optically readable synaptic modulators based on Tamm plasmon for adaptive multispectral image processing

Graphical abstract

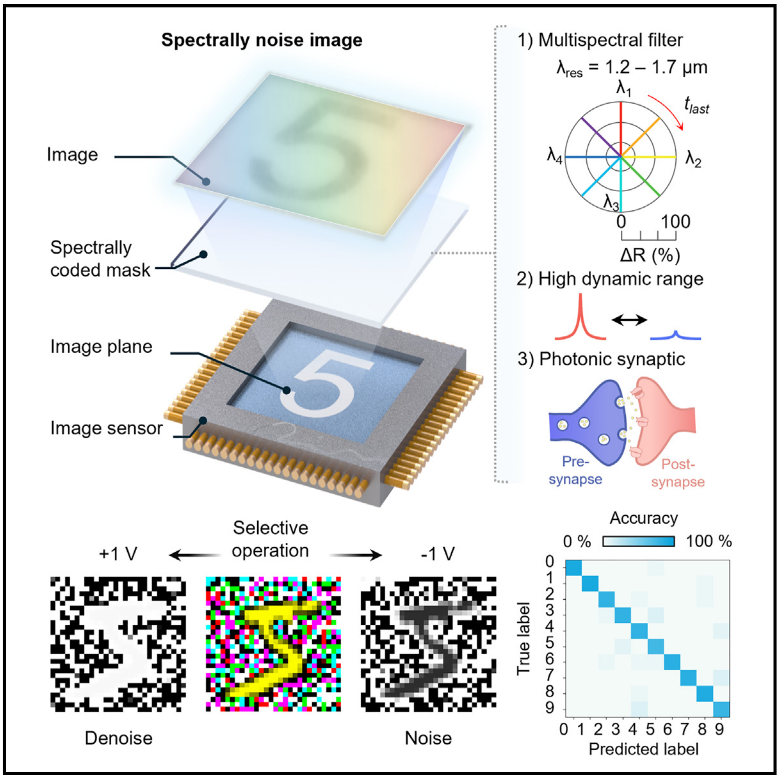

Authors

Joo Hwan Ko, Dong Hyun Seo, Se Yeon Kim, Yubin Lee, Kwangwook Park, Young Min Song

Correspondence

kwangwook.park@jbnu.ac.kr (K.P.), ymsong@gist.ac.kr (Y.M.S.)

In brief

Physics; Optics; Applied sciences

Highlights

- A multispectral free-space image processor using active Tamm plasmon resonators
- Tamm plasmon impedance matching allows precise wavelength tuning and adaptive control
- Stable multiple synaptic weights enable long-term memory for image processing tasks
- High Q-factor and tunability enhance denoising and spectral filtering performance

Ko et al., 2025, iScience *28*, 111800
February 21, 2025
https://doi.org/10.1016/j.isci.2025.111800

CellPress

iScience

CellPress OPEN ACCESS

Article

Optically readable synaptic modulators based on Tamm plasmon for adaptive multispectral image processing

Joo Hwan Ko,[1,7] Dong Hyun Seo,[1,7] Se Yeon Kim,[1,7] Yubin Lee,[1,7] Kwangwook Park,[2,3,4,*] and Young Min Song[1,5,6,8,*]
[1]School of Electrical Engineering and Computer Science, Gwangju Institute of Science and Technology, Gwangju 61005, Republic of Korea
[2]Division of Advanced Materials Engineering, Jeonbuk National University, Jeonju 54896, Republic of Korea
[3]Division of Electronic and Information Engineering, Jeonbuk National University, Jeonju 54896, Republic of Korea
[4]Hydrogen and Fuel Cell Research Center, Jeonbuk National University, Jeonju 54896, Republic of Korea
[5]Department of Semiconductor Engineering, Gwangju Institute of Science and Technology, Gwangju 61005, Republic of Korea
[6]AI Graduate School, Gwangju Institute of Science and Technology, Gwangju 61005, Republic of Korea
[7]These authors contributed equally
[8]Lead contact
*Correspondence: kwangwook.park@jbnu.ac.kr (K.P.), ymsong@gist.ac.kr (Y.M.S.)
https://doi.org/10.1016/j.isci.2025.111800

SUMMARY

The increasing demand for visual data processing reveals the limitations of traditional electronic systems in speed, energy efficiency, and adaptability. While optical computing offers a promising alternative, current systems often lack the flexibility required for multispectral and adaptive visual tasks. Here, we present an efficient way for highly adaptive, multispectral image filtering based on active Tamm plasmon resonators. We realize precise control over resonant wavelengths, enabling selective spectral targeting with high-quality factors. To achieve a gradual on/off function in the Tamm plasmon resonator, we integrate PEDOT:PSS, whose doping state modulates its metallic or dielectric properties. The partial doping of PEDOT:PSS allows for memorizing states, facilitating long-term potentiation and depression, and is essential for forming multiple synaptic states. By combining the high modulation depth, theoretically reaching 99%, with the non-volatile nature of PEDOT:PSS, we achieve stable multiple synaptic states with subtle saturation, resulting in 256 stable synaptic weights.

INTRODUCTION

The rapid advancement of computing technologies has emphasized the growing need for systems capable of efficiently processing and enhancing large volumes of visual data.[1] Traditional electronic computing architectures, while powerful, face increasing challenges in meeting the demands for speed, power consumption, and adaptability in image processing applications.[2–5] In response, neuromorphic computing—inspired by the brain's ability to process information through complex neuronal and synaptic functions—has emerged as a promising solution.[6] In this evolving stream, optical technologies have garnered significant interest for their ability to deliver superior speed and parallelism, making them well-suited for modern image processing tasks. Optical computing, particularly through photonic integrated circuits (PICs), integrates high-bandwidth optical communication with localized information processing, resulting in substantial improvements in processing speed and energy efficiency.[7–11] Additionally, diffractive deep neural networks (D^2NN), a form of free-space optical computing, efficiently process complex tasks by guiding light through diffractive layers, leveraging the speed, parallelism, and low energy consumption of optical systems.[12–14]

Beyond these innovations, reconfigurable photonic structures are increasingly recognized for their role as adaptive image filter layers in free-space optical sequences.[15–17] However, despite these advancements, further development is needed to address challenges such as denoising, spectral filtering, and contrast enhancement in multispectral data.[18] Enhancing the ability to address denoising, spectral filtering, and contrast enhancement could improve handling complex visual information. Nevertheless, current developments in reconfigurable free-space optical computing primarily focus on utilizing longer wavelength ranges, such as the gigahertz to terahertz spectrum, due to the complexity of system configurations required for active tuning.[19,20] Furthermore, integration with optical communication components targeting the near-infrared (NIR) range, such as optical fibers, photodetectors, and transceivers, will provide opportunities to enhance scalability and expand potential applications.[21–23]

Here, we present an approach utilizing active Tamm plasmon resonators, employing poly(3,4-ethylenedioxythiophene):polystyrene sulfonate (PEDOT:PSS) as electrically switchable material, distinguished by its NIR optical modulation capability, to develop a highly adaptable and efficient photonic structure for multispectral image processing.[24] PEDOT:PSS exhibits a tunable optical response, transitioning between metallic and dielectric properties depending on its doping state. This property allows for high absorptance or reflectance at wavelengths beyond its plasma frequency (λ_p = 1300 nm), making the NIR range particularly effective for optical modulation.[25–27] The partial doping behavior of PEDOT:PSS, where doped and undoped domains coexist, is critical for achieving long-term memory functions, enabling long-term potentiation and depression. These mechanisms are essential for forming multiple synaptic states, supporting neuromorphic computations across various signal (memory) stages.

First, we have engineered a reconfigurable device that offers fine control over the resonant wavelength by precisely adjusting the impedance matching condition of the Tamm plasmon resonator. This allows the resonator to have specific spectral components across a multispectral range with a high-quality factor (Q-factor).[27,28] To achieve adaptive controllability with a gradual on/off function in the Tamm plasmon resonator, we integrate PEDOT:PSS on the Tamm plasmon resonator.

For stable synaptic weights, we strategically combine the great modulation depth, theoretically reaching 99% in the Tamm plasmon, and the non-volatile properties of PEDOT:PSS, enabling the experimental realization of stable multiple synaptic states without saturation.[29] It results in the stability of 256 synaptic weights from continuous electrical pulse inputs. Also, the high Q-factor of Tamm plasmon ensures effective multispectral filtering without interference from unwanted signals, enabling the selective enhancement of target signals while suppressing unnecessary noise in dynamic environments (i.e., spatially and spectrally noisy patterns), paving the way for more efficient, scalable, and responsive technologies tailored to the complex demands of image processing.

RESULTS

Neuromorphic behavior of active Tamm plasmon and optical image denoising

Figure 1A illustrates the overall process of multispectral image denoising, achieved by harnessing the neuromorphic behavior of active Tamm plasmons. The selective multispectral neuromorphic mask can be fine-tuned to correspond with the target processing wavelength, effectively reducing noise and enhancing the clarity of spectrally multiplexed images. The spectrally tunable range covers the telecommunication range (λ_{res} = 1.2–1.7 μm) with a high dynamic range by modifying the thickness of the last layer (t_{last}) of distributed Bragg reflector (DBR) (see Figure 2). A key functionality is the realization of long-term potentiation and depression through active Tamm plasmons, where the calculated reflectance spectra exhibit significant intensity variations depending on the doping state of PEDOT:PSS with 99% modulation depth (Figure 1B). The Tamm plasmon structure is composed of a DBR, PEDOT:PSS, and a gold (Au) membrane, enabling strong light confinement within the cavity, which reflects multiple times, producing standing waves at specific resonance wavelengths (Figure 1C). Depending on the doping state of PEDOT:PSS, it can exhibit different complex refractive indices (between metallic and dielectric properties under doping (+1 V) and dedoping (−1 V) states, respectively, Figure S1). The metallic properties that effectively absorb incident light or dielectric properties that allow light to pass through, resulting in high absorptance/reflectance, respectively. While the thickness of PEDOT:PSS changes under sub-1-volt conditions, this variation has minimal impact on the absorption efficiency of the active Tamm plasmon structure (Figure S2).[30] The doping process of PEDOT:PSS, depicted in its chemical structure (Figure 1D), reveals the partially doped state induced by counterions and the coexistence of undoped domains.[31] This process is essential for the gradual tuning of optical properties. Additionally, the redox-based switching mechanism between PEDOT:PSS and the electrolyte medium shows the gradual and controlled modulation of the plasmonic response, which is critical for implementing neuromorphic functionalities (Figure 1E).[32,33]

Reflectance variation experiments demonstrate the ability to perform optical potentiation and depression at different wavelengths (1400 nm, 1500 nm, and 1600 nm) (Figure 1F). Applying specific electrical signals for controlled periods led to significant changes in reflectance, confirming the capacity for adaptive optical tuning. The voltage of each electrical signal during potentiation and depression (V_{pot}, V_{dep}) is applied for 1 s of triggered pulse and 1 s of relaxation. Finally, the contrast enhancement performed after varying numbers of pulse stimulations highlights the proficiency in optical potentiation and depression (Figure 1G). Dynamically adjusting the neuromorphic mask to the target wavelength improves image clarity and adapts to varying spectral conditions.

Computational modeling of multispectral active Tamm plasmon

In this section, we present a design flow for achieving reconfigurable photonic structures that operate efficiently across a multispectral range by precisely adjusting the last layer of a Tamm plasmon resonator. The proposed method offers a more efficient solution compared to conventional approaches, which frequently involve the use of complex nanophotonic structures to achieve high modulation depth across different spectral bands. Figure 2A provides a schematic of the active Tamm plasmon resonator used in our optical calculations, where the t_{last} is varied to control the resonant wavelength. As shown in Figure 2B, the reflectance spectra of different structures illustrate how adjusting t_{last}, particularly with PEDOT:PSS in its metallic state, significantly influences the resonant properties of the Tamm plasmon resonator. To achieve precise modifications of the last layer's thickness, we employed the glancing angle deposition (GLAD) technique using amorphous silicon (a-Si). The obliquely deposited medium provides an engineered porous medium, resulting in decreased refractive index. Also, it naturally forms a gradient film with gradually modulated thickness (Figure S3).[34–36] For the Tamm plasmon state to be established, the resonant wavelength (λ_{res}) must align with the center wavelength of the stop band, determined by the DBR. The thickness of the DBR layers was calculated using the quarter-wavelength condition in the medium, resulting in values of 259 nm for SiO_2 and 188 nm for Si_3N_4 at a resonance wavelength (λ_{res}) of 1500 nm. The thickness of the last layer (t_{last}), determined to be 83 nm, was calculated using the relation: $1 - r_{PEDOT:PSS}\, r_{DBR} \exp(2ikn_{last}t_{last}) \approx 0$, where $r_{PEDOT:PSS}$ is the reflection coefficient of a wave incident on the PEDOT:PSS and r_{DBR} is the reflection coefficient of a wave

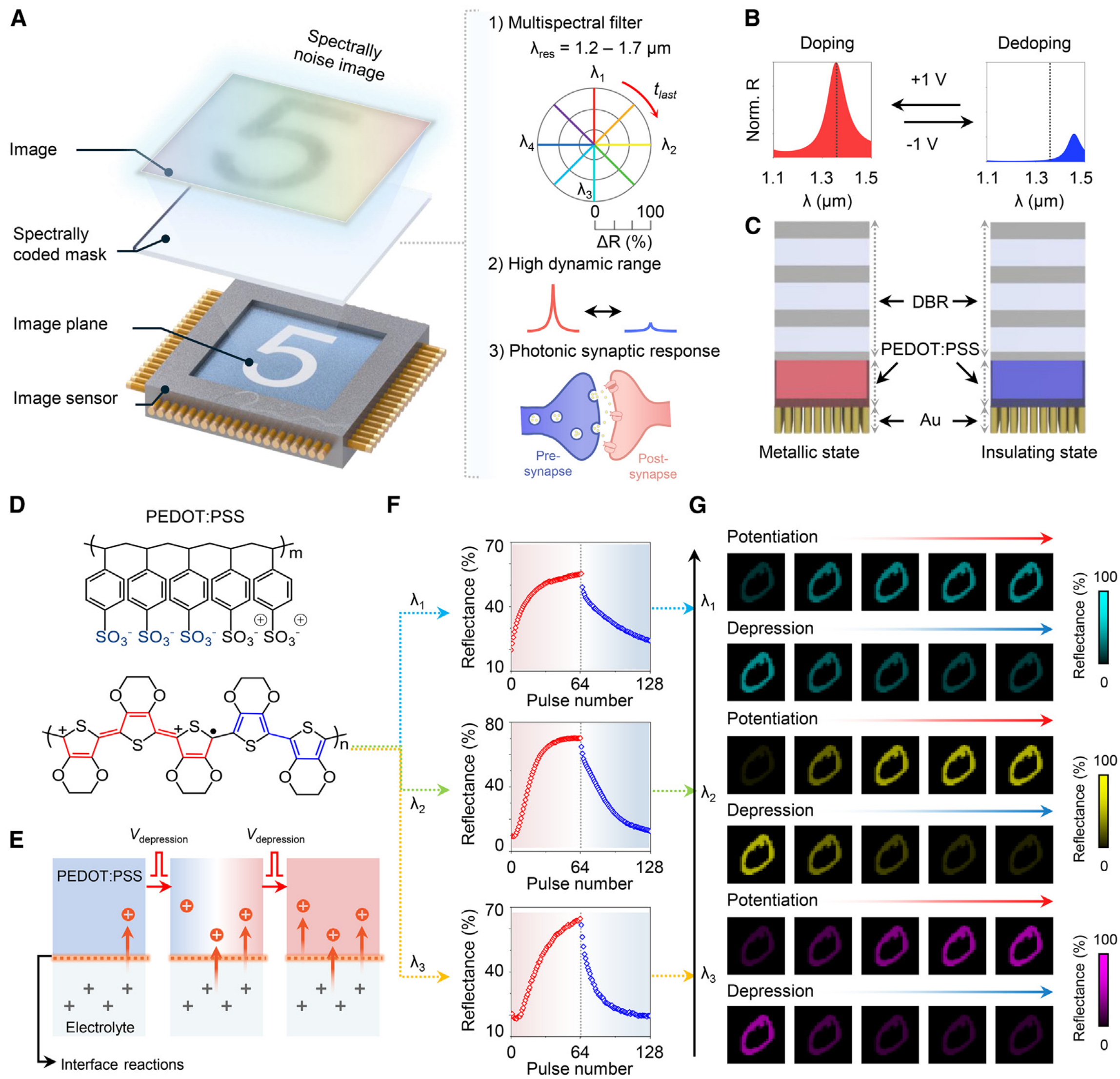

Figure 1. Overview of active Tamm plasmon-based optical neuromorphic computing for denoising function

(A) Schematics of the selective multispectral neuromorphic mask layer and denoising function.

(B) Calculated reflectance spectra of active Tamm plasmon at doped and dedoped state of poly(3,4-ethylenedioxythiophene):polystyrene sulfonate (PEDOT:PSS).

(C) Schematic of active Tamm plasmon composed of distributed Bragg reflector (DBR), PEDOT:PSS, and Au membrane.

(D) Chemical structure of PEDOT:PSS representing the partial doping of PEDOT:PSS by counterions and undoped domains.

(E) Schematic of redox-based switching with a counter-redox reaction between PEDOT:PSS and electrolyte medium.

(F) Reflectance variation representing optical potentiation and depression at different wavelengths of λ_1, λ_2, and λ_3 (1400 nm, 1500 nm, and 1600 nm). Voltage of each electrical signal (V_{pot}, V_{dep}) is applied for 1 s of triggered pulse and 1 s of relaxation.

(G) Contrast enhancement of reflectance images after 1, 16, 32, 48, and 64 pulse stimulations, demonstrating optical potentiation and depression.

incident on the DBR from Pr-Si last layer. Figure 2C illustrates a contour plot of absorptance as t_{last} varies from 0 to 900 nm. As shown, increasing t_{last} causes a shift in the resonance wavelength within the DBR stopband, centered around the target wavelength of 1500 nm. This adjustment allows for the precise tuning of the resonance wavelength of Tamm plasmon in the spectral range. Based on the results, we selected t_{last} values ranging from 0 to 140 nm to cover the optical communication band within the first-order Tamm plasmon state. Experimentally, the GLAD process was performed to gradually control the t_{last}.

The chemical structure of PEDOT:PSS in both its insulating and metallic states is shown in Figure 2D, along with the corresponding absorptance spectra. Finally, Figure 2E depicts the simulated electric field distribution and absorption profiles, which reveal strong confinement at the interface between the DBR and the PEDOT:PSS layer. This confinement ensures

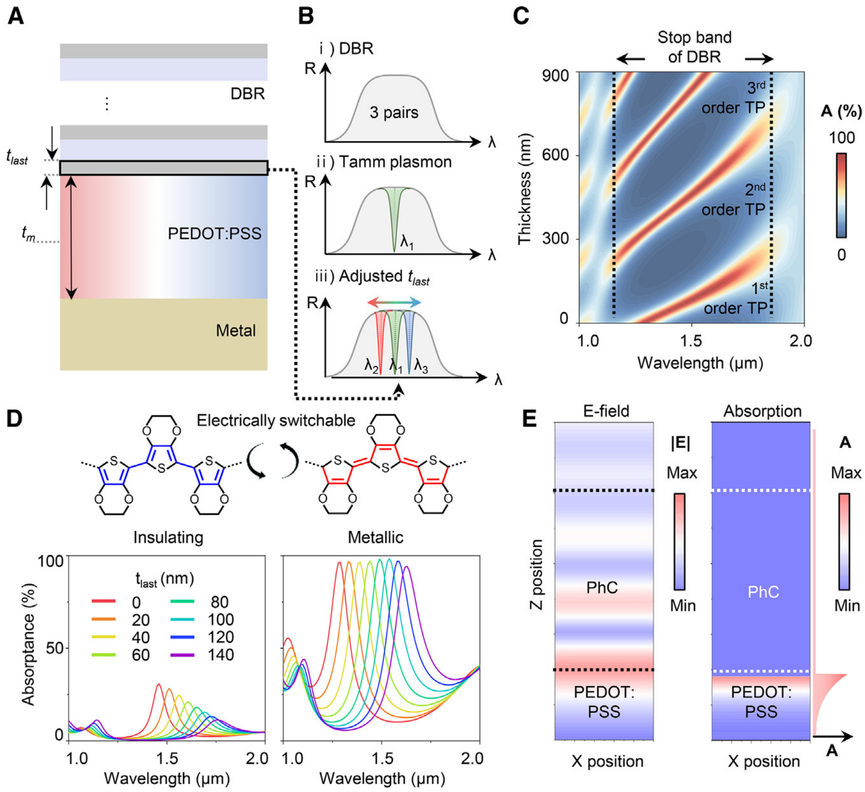

Figure 2. Structural analysis of active Tamm plasmon for multispectral operation

(A) Schematic depicting the active Tamm plasmon resonator. The thickness of last layer (t_{last}) is adjusted to control the wavelength of the Tamm plasmon.

(B) Illustration reflectance spectra under the different structures (i, DBR; ii, Tamm plasmon with fixed t_{last}, and iii, Tamm plasmon with adjusted t_{last}). The doping state of PEDOT:PSS is fixed with a metallic state.

(C) Absorptance contour of Tamm plasmon by modifying the t_{last} from 0 to 900 nm

(D) Chemical structure of PEDOT:PSS at the insulating and metallic state, respectively (top). Absorptance spectra at the insulating and metallic state of PEDOT:PSS with different t_{last} (bottom).

(E) Simulated electric field (left) and absorption profile (right) using the PEDOT:PSS in its metallic state at the Tamm plasmon wavelength.

efficient absorption at the Tamm plasmon wavelength. Overall, this method provides an effective solution for achieving high modulation depth and reconfigurability across a broad spectral range (Figure S4).

Optical synaptic behaviors of multispectral optical synaptic resonator across broadband target wavelengths

Partial oxidation and reduction mechanisms based on electrochemical reactions enable the optical synaptic behavior of MOSR.[32,33] As shown in Figure 3A, we can induce gradual optical modulation by controlling the flow of ions between the electrolyte and device through the applied working electrode (WE) and counter electrode (CE). The active Tamm plasmon shows great modulation depth reaching 99%, also, it is confirmed experimentally around 78% at the designed target wavelength, λ_{res} = 1550 nm, estimated to have a Pr-Si thickness of 95 nm (Figures 3B and S5). Additionally, we experimentally achieved a considerable modulation depth across a broad wavelength range from 1380 nm to 1600 nm (Figure S5). The redox reaction can be clearly observed from the cyclic voltammetry plot of the MOSR, with the porous layer shown in the red line and the dense layer in the blue line. The peak current of the MOSR with porous Au is higher than that of the dense Au electrode, indicating enhanced ion exchange through the Au nanocolumns (Figure S6). Additionally, the porosity of Au has minimal influence on the optical efficiency, ensuring consistent performance across varying porosities. (Figure S7). Biological synapses generate excitatory and inhibitory postsynaptic potentials (EPSP and IPSP) depending on the type of neurotransmitter involved.[37–39] This mechanism is similarly observed in neuromorphic devices, where the output behavior varies based on excitatory and inhibitory input pulses, indicating the potential for synaptic weight adjustment within the device. Such characteristics enable weight-based learning in the neuromorphic computing process, allowing for the modulation of synaptic weights.[40] Therefore, neuromorphic devices, which mimic the operational principles of biological synapses, possess the potential to evolve into systems with efficient information processing and learning capabilities. Figure 3C illustrates the optical synaptic characteristics of EPSP and IPSP confirmed at the three target wavelengths (Figures S8 and S9). The excitatory and inhibitory voltages of −1 V and 1 V with pulse widths and a time interval of 1 s, respectively. Optical EPSP and IPSP were confirmed across all three wavelengths, revealing distinct potentiated/depressed characteristics in response to consecutive inputs, indicative of paired-pulse facilitation (PPF) behavior. To investigate the PPF behavior more closely, the PPF index is measured at different time intervals, from 1 s to 30 s, in Figure 3D (Figure S10). It was observed that as the time interval increases at all target wavelengths, the degree of influence from the preceding input diminishes, demonstrating normal PPF behavior.[41] Notably, PEDOT:PSS-based Tamm plasmon resonator exhibits non-volatile behavior between electrochemical oxidation and reduction, leading to prolonged attenuation characteristics. The PPF index exceeded 100% for relatively long durations, up to approximately 30 s, indicating a sustained influence from the preceding input. The gradual modulation of optical synaptic weights, induced by continuous electrical input signals, enables the active Tamm plasmon resonator to display long-term potentiation (LTP) and long-term depression (LTD) characteristics. Figure 3E shows reflectance corresponding to 256 electrical pulses at the target wavelength of 1500 nm for both LTP and LTD, induced by an

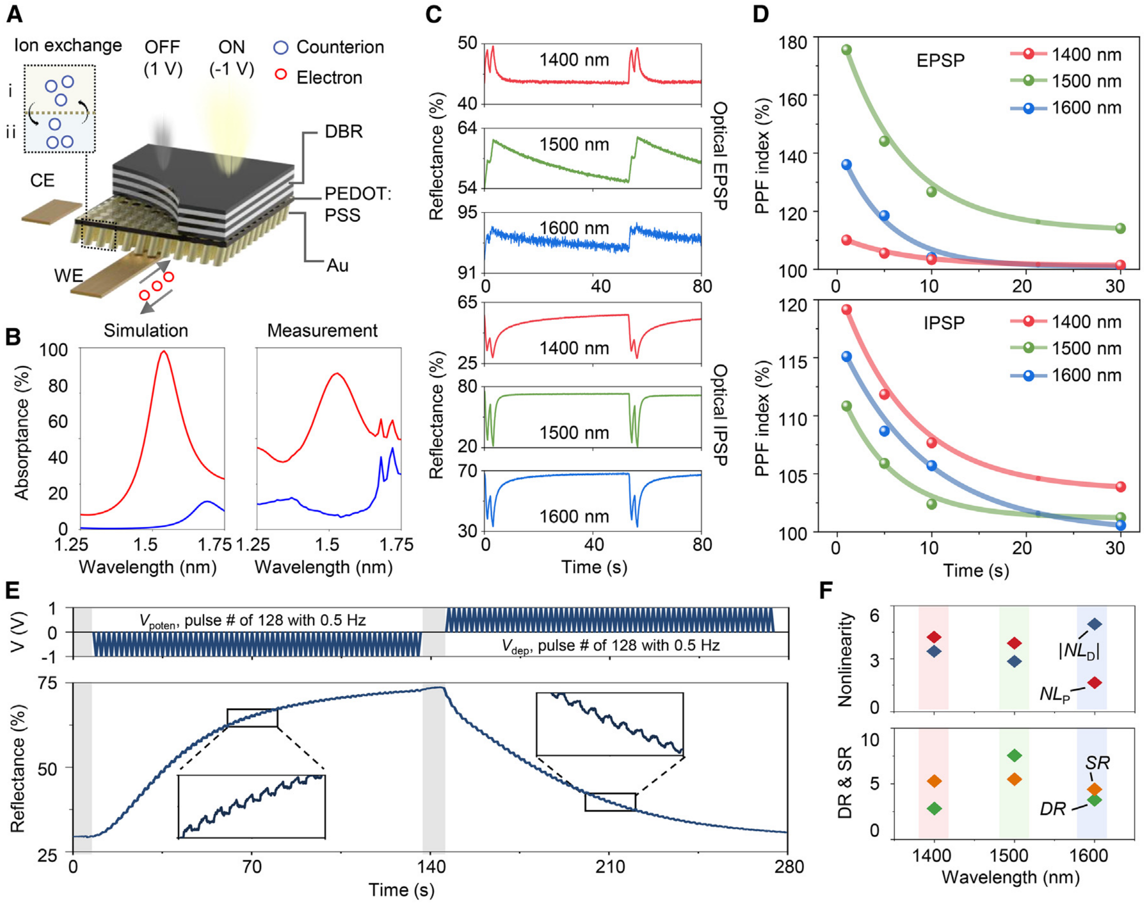

Figure 3. Measurement of optical synaptic characteristics at designed target wavelengths

(A) Schematic of a proposed multispectral optical synaptic resonator (MOSR). The inset image shows i) PEDOT:PSS and ii) electrolyte medium. The counterions are exchanged across Au membrane.

(B) Simulated and measured absorption spectra of Tamm plasmon resonator with metallic state of PEDOT:PSS. The blue and red lines show the oxidized and reduced states, respectively.

(C) Measured reflectance representing optical excitatory/inhibitory postsynaptic potential (EPSP/IPSP) response.

(D) Calculated paired-pulse facilitation (PPF) index with optical EPSP and IPSP.

(E) Long-term potentiation/depression (LTP/LTD) showing 256 discrete states under the electrical pulse of 0.5 Hz. Two insets provide a magnified view of the individual states.

(F) Synaptic parameters, nonlinearity (NL), dynamic range (DR), and symmetric ratio (SR), at three target wavelengths.

electrical input of 1 V at 0.5 Hz. The inset image displays distinct individual states, confirming the non-volatile characteristics of the system. Based on the experimental results measured at the three target wavelengths, calculations were performed for synaptic parameters including nonlinearity (NL), dynamic range (DR), and symmetry ratio (SR) (Figures 3F, S11, and S12).[42]

Multispectral data processing capabilities of multispectral optical synaptic resonator for optical neuromorphic systems

Figure 4A illustrates the schematic for multispectral image denoising using the proposed multispectral optical synaptic resonator (MOSR) filter.[43] Separating the image and noise regions and forming spatial alignment between the image at the target wavelengths and the resonator is a significant challenge.[22] However, by introducing sub-pixel structures, we can achieve efficient multispectral image processing without requiring precise spatial alignment between the multiplexed image and each cell of the MOSR-filter array.[44,45] The MOSR demonstrated the selective processing of broadband multispectral data due to its high Q-factor (∼14) and significant modulation depth. A 28 × 28 pixel multispectral MNIST dataset, intentionally corrupted with noise across various wavelengths, was used in this study.[46] Target wavelengths encoded the MNIST handwritten digit, while non-target wavelengths were considered background noise. By illuminating the noisy multispectral pattern onto the MOSR filter and adjusting reflectance through electrical inputs, the obscured information in the target wavelengths selectively appeared. The processed data were classified using a neural network model, evaluating the MOSR's ability to process multispectral noise patterns selectively (Figure S13).[47,48]

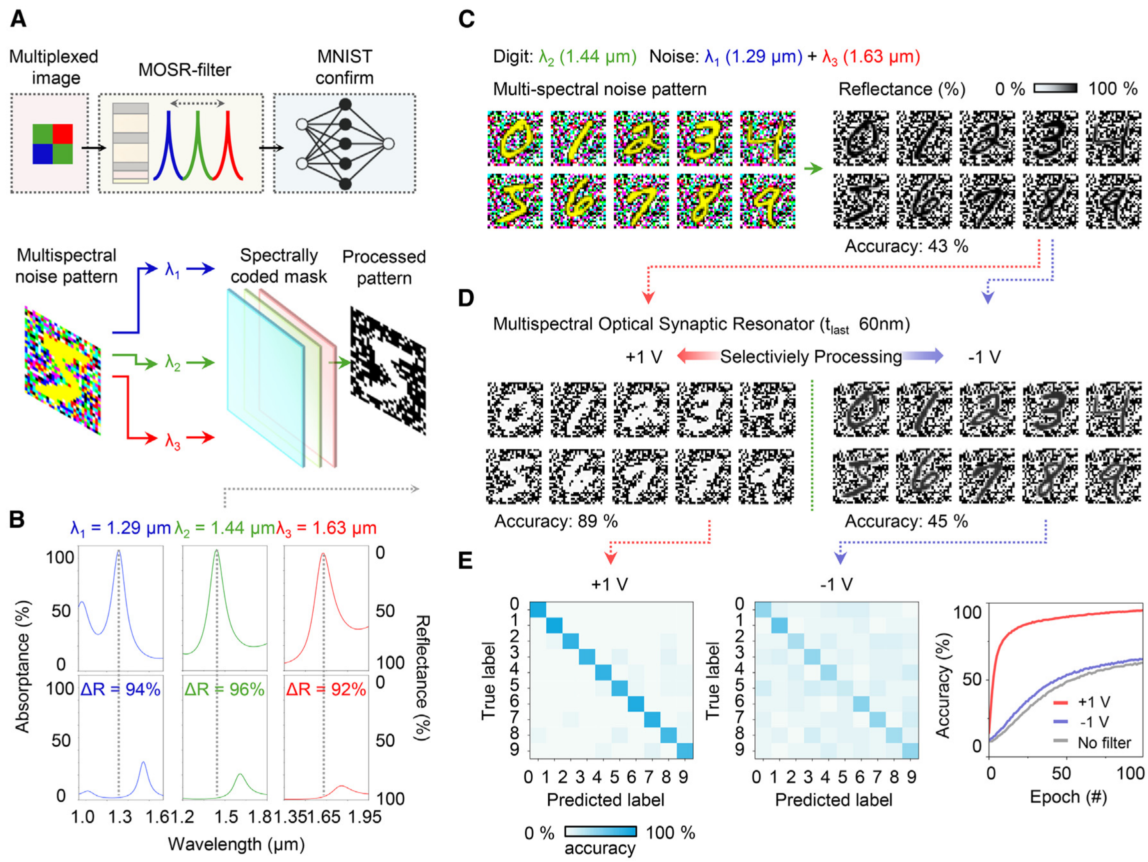

Figure 4. Multispectral image processing based on optical synaptic characteristics

(A) Schematic and process flow for multispectral image processing using the MOSR filter.

(B) Calculated absorption spectra for multispectral image denoising and recognition. λ_1, λ_2, and λ_3 represent resonant wavelengths of 1.29 μm, 1.44 μm, and 1.63 μm, respectively.

(C) MNIST handwritten input image with background noise. The digits have resonant wavelength λ_2, while λ_1 and λ_3 are applied as background noise.

(D) Multispectral image processing using the MOSR filter, designed at the resonant wavelength of 1.44 μm (λ_2).

(E) Multispectral image classification and predicted result using a neural network.

For this simulation, three resonant wavelengths (λ_1 = 1.29 μm, λ_2 = 1.44 μm, and λ_3 = 1.63 μm) were selected from the calculated absorption spectra. The absorption characteristics of the MOSR were analyzed as a function of t_{last}, at 0 nm, 60 nm, and 140 nm in both metallic and insulating states (Figure 4B). In the dedoped insulating state (−1 V), the MOSR exhibited high reflectance. Upon applying an electrical input, the MOSR transitioned to the metallic state (+1 V), triggering Tamm plasmon resonance, which led to significant absorption at the target wavelengths, reducing reflectance to near-zero. The MOSR devices with three resonant wavelengths of λ_1, λ_2, and λ_3 demonstrated optical synaptic weight modulation of 94%, 96%, and 92%, respectively. This confirms that the device's reflectance can be electrically switched between the insulating and metallic states.

Figure 4C displays the input MNIST handwritten digit at the three resonant wavelengths. The digits were represented at λ_2, while gaussian-distribution noise with a factor of 30 was applied at λ_1 and λ_3.[49–51] For visualization, λ_1 was mapped to cyan, λ_2 to yellow, and λ_3 to magenta. The multispectral noise pattern was initially converted into a reflectance dataset, assuming complete reflectance (100%) across all wavelengths. Prior to MOSR filtering, classification accuracy for the multispectral noise pattern was 61.2%, making MNIST digit recognition infeasible. After passing through the MOSR filter with a t_{last} of 60 nm (Figure 4D), the target wavelength (λ_2), corresponding to the digit region exhibited strong resonance. This resonance allowed the MOSR to fully absorb λ_2, reducing its reflectance to nearly zero and demonstrating its capability for effective selective information processing. Due to the high Q-factor, the reflectance of non-target wavelengths (λ_1 and λ_3) remained stable, while the reflectance of the target wavelength (λ_2) was precisely modulated. Following the application of +1 V to the MOSR filter, classification accuracy improved significantly to 95.3%. After 100 epochs of training, filtering led to a 34.1% increase in accuracy for λ_2. Additional reflectance simulations based on data for the three t_{last} MOSR further validated the outcomes. The other resonant wavelengths, λ_1 and λ_3, showed accuracy improvement of 34.2% and 34.1%, respectively, compared to the non-filtered condition (Figure S14). Conversely, applying −1 V can obscure the digit information, reducing accuracy to 63.6%, and rendering the digits nearly unrecognizable. This demonstrates the efficacy of the MOSR in selective information processing. The confusion matrix for MNIST classification after 100 training epochs is shown in Figure 4E. The results confirm that effective information extraction and selective in-sensor processing can be achieved with low-power operation using the MOSR filter.

DISCUSSION

In conclusion, we have developed a highly adaptable multispectral free-space image processing system that focuses on denoising using active Tamm plasmon resonators operating under sub-1-volt conditions. The precise impedance matching allows for selective spectral processing, providing a design strategy for selective wavelengths for efficient noise reduction across a wide multispectral range. Its tunability, coupled with neuromorphic capabilities such as long-term potentiation and depression, enables adaptive modulation and high-performance filtering, making it well-suited for complex image processing tasks. Additionally, we demonstrated the stability of 256 synaptic weights from continuous electrical pulse inputs based on the high modulation depth of the active Tamm plasmon resonator and the non-volatile memory property of PEDOT:PSS, showcasing long-term memory and non-volatile behavior. Also, a high Q-factor ensures effective multispectral filtering without interference from unwanted signals. The partial doping of PEDOT:PSS facilitates dynamic transitions between metallic and dielectric states, further enhancing its responsiveness to varying spectral conditions. This adaptability not only improves noise reduction but also significantly enhances spectral filtering and contrast, representing a major advancement in optical computing technologies.

Looking forward, we envision our suggestion providing a foundation for adaptable free-space optical computing. By integrating a variety of optically active materials, the platform can be customized to suit specific target applications, allowing for the appropriate selection and use of materials based on the desired functionality.[52–56] Additionally, with further integration of interconnected configurations, such as addressable diffractive filters, the proposed platform could support advancements in real-time data processing, autonomous systems, and immersive visual technologies. Also, these features align with the requirements of advanced imaging systems, such as biomimetic vision models, which demand precise spectral filtering and high contrast in dynamic environments.[57,58] The resonator enhances multispectral imaging by isolating diagnostically relevant wavelengths, improving signal-to-noise ratios, and facilitating the detection of subtle biomarkers, leading to better outcomes in advanced endoscopic applications and early cancer detection.[59–61] Its compact, energy-efficient design supports integration into portable diagnostic platforms, enabling minimally invasive procedures, point-of-care diagnostics, and real-time adaptive imaging systems.[62]

Limitations of the study

The current study encounters integration limitations due to the reflective filtering structure employed to achieve the high-Q Tamm plasmon on/off state. From an image processing standpoint, two primary constraints arise: (1) the relay of components within the system, and (2) the expansion of the operational spectral range with diverse tuning devices. These challenges underscore the need for further development to facilitate seamless integration and broader spectral adaptability in future applications.[18] Additionally, the planar surface of the Tamm plasmon resonator provides only intensity modulation, limiting the system's ability to form high-dimensional interconnections with multiple filters. The complex modulation of light, including both intensity and phase, with adaptive functionality may significantly enhance diffractive interconnections in free-space computational systems.[16,63] The advancement of diffractive interconnections with synaptic characteristics could significantly enhance the potential for adaptive image processing without the need for post-processing. Contamination and fabrication inconsistencies further challenge the reliability and reproducibility of PEDOT:PSS-based systems. Scattering-type Scanning Near-Field Optical Microscopy (s-SNOM) offers nanometric resolution for mapping permittivity and refractive index, making it an effective tool for nanoscale chemical imaging, plasmonic effect observation, and defect analysis in thin films.[64–66] Integrating s-SNOM into fabrication processes can provide real-time feedback, enabling precise adjustments, improving material uniformity, and reducing variability. These measures are critical for ensuring consistent performance and scalability in future applications. Despite these limitations, the proposed system establishes a foundation for scalable and energy-efficient optical image processing. Future research will focus on improving component relay architecture and expanding the spectral range, with the next step likely heading toward addressable diffractive structures for enhanced functionality.

RESOURCE AVAILABILITY

Lead contact

Requests for further information and resources should be directed to and will be fulfilled by Young Min Song, (ymsong@gist.ac.kr.).

Materials availability

This study did not generate new unique reagents.

Data and code availability

All data reported in this article will be shared by the lead contact upon request. This article does not report the original code. Any additional information required to reanalyze the data reported in this article is available from the lead contact upon request.

ACKNOWLEDGMENTS

This work was supported by the GIST Research Institute (GRI) RISE and GIST-MIT Research Collaboration through a grant funded by the GIST and National Research Foundation of Korea (NRF) funded by the Ministry of Science and ICT (2023R1A2C3004531, 2021M3H4A1A04086357). This material is also partly based upon work supported by the International Technology Center Indo-Pacific (ITC IPAC) and Army Research Office, under Contract No. FA5209-22-P-0162. K.P. also recognizes the support from the National Research Foundation of Korea (NRF) grant funded by the Korean government (MSIT) (NRF-2022R1F1A1064130). J.H.K. acknowledges the support from the AI-based GIST Research Scientist Project and NRF (RS-2024-00345558). This work was supported by the Technology Innovation Program (or Industrial Strategic Technology Development Program- Bio-industry Technology Development Project) (RS-2024-00467230, Development of a Digital Healthcare

Device for the Non-invasive Continuous Monitoring of Myocardial Infarction Biomarkers Based on Mid-Infrared Nano-Optical Filters) funded By the Ministry of Trade Industry & Energy (MOTIE, Korea).

AUTHOR CONTRIBUTIONS

Conceptualization, Y.M.S., K.P., J.H.K., and D.H.S.; methodology, J.H.K and D.H.S.; computation, J.H.K., D.H.S., and Y.L.; investigation, J.H.K and S.Y.K.; formal analysis, J.H.K., D.H.S., S.Y.K., and Y.L.; writing – original draft, J.H.K., D.H.S., and Y.L.; writing–review and editing, S.Y.K., Y.L., K.P., and Y.M.S.; funding acquisition, Y.M.S., K.P., and J.H.K.; supervision, Y.M.S.

DECLARATION OF INTERESTS

The authors declare no competing interests. The author does not have any commercial or associative interest that represents a conflict of interest in connection with the work submitted.

STAR★METHODS

Detailed methods are provided in the online version of this paper and include the following:

- KEY RESOURCES TABLE
- METHOD DETAILS
  - Optical simulation
  - Optical characterization and measurement
  - Electrochemical setup and measurement
  - Fabrication of active Tamm plasmon
  - Neural network simulation and implementation
  - Porosity modulation based on volume averaging theory (VAT)
  - Weight nonlinearity model
  - Symmetricity calculation
  - Paired-pulsed facilitation equation

SUPPLEMENTAL INFORMATION

Supplemental information can be found online at https://doi.org/10.1016/j.isci.2025.111800.

Received: September 9, 2024
Revised: October 22, 2024
Accepted: January 9, 2025
Published: January 11, 2025

REFERENCES

1. Zhou, F., and Chai, Y. (2020). Near-sensor and in-sensor computing. Nat. Electron. *3*, 664–671.
2. Zhou, F., Zhou, Z., Chen, J., Choy, T.H., Wang, J., Zhang, N., Lin, Z., Yu, S., Kang, J., Wong, H.-S.P., and Chai, Y. (2019). Optoelectronic resistive random access memory for neuromorphic vision sensors. Nat. Nanotechnol. *14*, 776–782.
3. Roy, K., Jaiswal, A., and Panda, P. (2019). Towards spike-based machine intelligence with neuromorphic computing. Nature *575*, 607–617.
4. Zidan, M.A., Strachan, J.P., and Lu, W.D. (2018). The future of electronics based on memristive systems. Nat. Electron. *1*, 22–29.
5. Burr, G.W., Shelby, R.M., Sebastian, A., Kim, S., Kim, S., Sidler, S., Virwani, K., Ishii, M., Narayanan, P., Fumarola, A., et al. (2017). Neuromorphic computing using non-volatile memory. Adv. Phys. X *2*, 89–124.
6. Preissl, R., Wong, T.M., Datta, P., Flickner, M., Singh, R., Esser, S.K., Risk, W.P., Simon, H.D., and Modha, D.S. (2012). Compass: A Scalable Simulator for an Architecture for Cognitive Computing (IEEE), pp. 1–11.
7. Shastri, B.J., Tait, A.N., Ferreira de Lima, T., Pernice, W.H.P., Bhaskaran, H., Wright, C.D., and Prucnal, P.R. (2021). Photonics for artificial intelligence and neuromorphic computing. Nat. Photonics *15*, 102–114.
8. Feldmann, J., Youngblood, N., Wright, C.D., Bhaskaran, H., and Pernice, W.H.P. (2019). All-optical spiking neurosynaptic networks with self-learning capabilities. Nature *569*, 208–214.
9. Feldmann, J., Youngblood, N., Karpov, M., Gehring, H., Li, X., Stappers, M., Le Gallo, M., Fu, X., Lukashchuk, A., Raja, A.S., et al. (2021). Parallel convolutional processing using an integrated photonic tensor core. Nature *589*, 52–58.
10. Churaev, M., Wang, R.N., Riedhauser, A., Snigirev, V., Blésin, T., Möhl, C., Anderson, M.H., Siddharth, A., Popoff, Y., Drechsler, U., et al. (2023). A heterogeneously integrated lithium niobate-on-silicon nitride photonic platform. Nat. Commun. *14*, 3499.
11. Wang, C., Zhang, M., Chen, X., Bertrand, M., Shams-Ansari, A., Chandrasekhar, S., Winzer, P., and Lončar, M. (2018). Integrated lithium niobate electro-optic modulators operating at CMOS-compatible voltages. Nature *562*, 101–104.
12. Lin, X., Rivenson, Y., Yardimci, N.T., Veli, M., Luo, Y., Jarrahi, M., and Ozcan, A. (2018). All-optical machine learning using diffractive deep neural networks. Science *361*, 1004–1008.
13. Qian, C., Lin, X., Lin, X., Xu, J., Sun, Y., Li, E., Zhang, B., and Chen, H. (2020). Performing optical logic operations by a diffractive neural network. Light Sci. Appl. *9*, 59.
14. Mengu, D., Tabassum, A., Jarrahi, M., and Ozcan, A. (2023). Snapshot multispectral imaging using a diffractive optical network. Light Sci. Appl. *12*, 86.
15. Zuo, Y., Li, B., Zhao, Y., Jiang, Y., Chen, Y.-C., Chen, P., Jo, G.-B., Liu, J., and Du, S. (2019). All-optical neural network with nonlinear activation functions. Optica *6*, 1132–1137.
16. Liu, C., Ma, Q., Luo, Z.J., Hong, Q.R., Xiao, Q., Zhang, H.C., Miao, L., Yu, W.M., Cheng, Q., Li, L., and Cui, T.J. (2022). A programmable diffractive deep neural network based on a digital-coding metasurface array. Nat. Electron. *5*, 113–122.
17. An, S., Zheng, B., Julian, M., Williams, C., Tang, H., Gu, T., Zhang, H., Kim, H.J., and Hu, J. (2022). Deep neural network enabled active metasurface embedded design. Nanophotonics *11*, 4149–4158.
18. Xu, Y., Shi, Y., Qian, C., Xie, P., Jin, C., Shi, X., Zhang, G., Liu, W., Wan, C., Ho, J.C., et al. (2023). Optically readable organic electrochemical synaptic transistors for neuromorphic photonic image processing. Nano Lett. *23*, 5264–5271.
19. Kindness, S.J., Almond, N.W., Wei, B., Wallis, R., Michailow, W., Kamboj, V.S., Braeuninger-Weimer, P., Hofmann, S., Beere, H.E., Ritchie, D.A., and Degl'Innocenti, R. (2018). Active control of electromagnetically induced transparency in a terahertz metamaterial array with graphene for continuous resonance frequency tuning. Adv. Opt. Mater. *6*, 1800570.
20. Nagatsuma, T., Ducournau, G., and Renaud, C.C. (2016). Advances in terahertz communications accelerated by photonics. Nat. Photonics *10*, 371–379.
21. Kaushal, H., and Kaddoum, G. (2017). Optical communication in space: Challenges and mitigation techniques. IEEE Commun. Surv. Tutorials *19*, 57–96.
22. Hu, J., Mengu, D., Tzarouchis, D.C., Edwards, B., Engheta, N., and Ozcan, A. (2024). Diffractive optical computing in free space. Nat. Commun. *15*, 1525.
23. Vanyukov, V.V., Mikheev, G.M., Mogileva, T.N., Puzyr, A.P., Bondar, V.S., and Svirko, Y.P. (2015). Near-IR nonlinear optical filter for optical communication window. Appl. Opt. *54*, 3290–3293.
24. Elschner, A., Kirchmeyer, S., Lovenich, W., Merker, U., and Reuter, K. (2010). PEDOT: Principles and Applications of an Intrinsically Conductive Polymer (CRC press).

25. Karst, J., Floess, M., Ubl, M., Dingler, C., Malacrida, C., Steinle, T., Ludwigs, S., Hentschel, M., and Giessen, H. (2021). Electrically switchable metallic polymer nanoantennas. Science *374*, 612–616.
26. Karst, J., Lee, Y., Floess, M., Ubl, M., Ludwigs, S., Hentschel, M., and Giessen, H. (2022). Electro-active metaobjective from metalenses-on-demand. Nat. Commun. *13*, 7183.
27. Ko, J.H., Seo, D.H., Jeong, H.H., Kim, S., and Song, Y.M. (2024). Sub-1-volt electrically programmable optical modulator based on active Tamm plasmon. Adv. Mater. *36*, 2310556.
28. Kim, S.H., Ko, J.H., Yoo, Y.J., Kim, M.S., Lee, G.J., Ishii, S., and Song, Y.M. (2022). Single-Material, Near-Infrared Selective Absorber Based on Refractive Index-Tunable Tamm Plasmon Structure. Adv. Opt. Mater. *10*, 2102388.
29. Van De Burgt, Y., Lubberman, E., Fuller, E.J., Keene, S.T., Faria, G.C., Agarwal, S., Marinella, M.J., Alec Talin, A., and Salleo, A. (2017). A non-volatile organic electrochemical device as a low-voltage artificial synapse for neuromorphic computing. Nat. Mater. *16*, 414–418.
30. Doshi, S., Ji, A., Mahdi, A.I., Keene, S.T., Selvin, S.P., Lalanne, P., Appel, E.A., Melosh, N.A., and Brongersma, M.L. (2024). Electrochemically mutable soft metasurfaces. Nat. Mater. https://doi.org/10.1038/s41563-024-02042-4.
31. Liang, Y., Offenhäusser, A., Ingebrandt, S., and Mayer, D. (2021). PEDOT: PSS-based bioelectronic devices for recording and modulation of electrophysiological and biochemical cell signals. Adv. Healthcare Mater. *10*, 2100061.
32. van De Burgt, Y., Melianas, A., Keene, S.T., Malliaras, G., and Salleo, A. (2018). Organic electronics for neuromorphic computing. Nat. Electron. *1*, 386–397.
33. Rivnay, J., Inal, S., Salleo, A., Owens, R.M., Berggren, M., and Malliaras, G.G. (2018). Organic electrochemical transistors. Nat. Rev. Mater. *3*, 17086.
34. Yoo, Y.J., Kim, W.G., Ko, J.H., Kim, Y.J., Lee, Y., Stanciu, S.G., Lee, J.M., Kim, S., Oh, J.W., and Song, Y.M. (2020). Large-area virus coated ultrathin colorimetric sensors with a highly lossy resonant promoter for enhanced chromaticity. Adv. Sci. *7*, 2000978.
35. Ko, J.H., Yoo, Y.J., Kim, Y.J., Lee, S.S., and Song, Y.M. (2020). Flexible, large-area covert polarization display based on ultrathin lossy nanocolumns on a metal film. Adv. Funct. Mater. *30*, 1908592.
36. Yoo, Y.J., Ko, J.H., Kim, W.-G., Kim, Y.J., Kong, D.-J., Kim, S., Oh, J.-W., and Song, Y.M. (2020). Dual-mode colorimetric sensor based on ultrathin resonating facilitator capable of nanometer-thick virus detection for environment monitoring. ACS Appl. Nano Mater. *3*, 6636–6644.
37. Kirkwood, A., Rioult, M.C., and Bear, M.F. (1996). Experience-dependent modification of synaptic plasticity in visual cortex. Nature *381*, 526–528.
38. Yang, R., Huang, H.M., and Guo, X. (2019). Memristive synapses and neurons for bioinspired computing. Adv. Electron. Mater. *5*, 1900287.
39. Bear, M., Connors, B., and Paradiso, M. (2006). Neuroscience: Exploring the Brain (Lippincott Williams & Wilkins), p. 411.
40. Ohno, T., Hasegawa, T., Tsuruoka, T., Terabe, K., Gimzewski, J.K., and Aono, M. (2011). Short-term plasticity and long-term potentiation mimicked in single inorganic synapses. Nat. Mater. *10*, 591–595.
41. Lee, K.-C., Li, M., Chang, Y.-H., Yang, S.-H., Lin, C.-Y., Chang, Y.-M., Yang, F.-S., Watanabe, K., Taniguchi, T., Ho, C.-H., et al. (2020). Inverse paired-pulse facilitation in neuroplasticity based on interface-boosted charge trapping layered electronics. Nano Energy *77*, 105258.
42. Chen, P.-Y., Peng, X., and Yu, S. (2017). NeuroSim+: An Integrated Device-To-Algorithm Framework for Benchmarking Synaptic Devices and Array Architectures (IEEE), pp. 6.1. 1–6.1. 4.
43. Islam, M.M., Rahman, M.S., Heldmyer, H., Han, S.S., Jung, Y., and Roy, T. (2024). Bio-inspired "Self-denoising" capability of 2D materials incorporated optoelectronic synaptic array. npj 2D Mater. Appl. *8*, 21.
44. Kim, I., Jang, J., Kim, G., Lee, J., Badloe, T., Mun, J., and Rho, J. (2021). Pixelated bifunctional metasurface-driven dynamic vectorial holographic color prints for photonic security platform. Nat. Commun. *12*, 3614.
45. Wang, Z., Dai, C., Zhang, J., Wang, D., Shi, Y., Wang, X., Zheng, G., Zhang, X., and Li, Z. (2022). Real-time tunable nanoprinting-multiplexing with simultaneous meta-holography displays by stepwise nanocavities. Adv. Funct. Mater. *32*, 2110022.
46. Deng, L. (2012). The mnist database of handwritten digit images for machine learning research [best of the web]. IEEE Signal Process. Mag. *29*, 141–142.
47. Hecht-Nielsen, R. (1992). Theory of the backpropagation neural network. In Neural networks for perception (Elsevier), pp. 65–93.
48. Lippmann, R.P. (1989). Pattern classification using neural networks. IEEE Commun. Mag. *27*, 47–50.
49. Luisier, F., Blu, T., and Unser, M. (2011). Image denoising in mixed Poisson–Gaussian noise. IEEE Trans. Image Process. *20*, 696–708.
50. Russo, F. (2003). A method for estimation and filtering of Gaussian noise in images. IEEE Trans. Instrum. Meas. *52*, 1148–1154.
51. Deng, G., and Cahill, L. (1993). An Adaptive Gaussian Filter for Noise Reduction and Edge Detection (IEEE), pp. 1615–1619.
52. Ko, J.H., Yeo, J.-E., Jeong, H.E., Kim, H.M., Yoo, Y.J., Yuk, Y., Lee, S., and Song, Y.M. (2024). Switchable and Conspicuous Retroreflective Sensors Inspired by the Wing Scale of an Emerald Swallowtail. Biosens. Bioelectron. *260*, 116445.
53. Ko, J.H., Yeo, J.-E., Jeong, H.E., Yoo, D.E., Lee, D.W., Oh, Y.-W., Jung, S., Kang, I.-S., Jeong, H.-H., and Song, Y.M. (2024). Electrochromic nanopixels with optical duality for optical encryption applications. Nanophotonics *13*, 1119–1129.
54. Prabhathan, P., Sreekanth, K.V., Teng, J., Ko, J.H., Yoo, Y.J., Jeong, H.-H., Lee, Y., Zhang, S., Cao, T., and Popescu, C.-C. (2023). Roadmap for phase change materials in photonics and beyond. iScience *26*, 107946.
55. Ko, J.H., Yoo, Y.J., Lee, Y., Jeong, H.-H., and Song, Y.M. (2022). A review of tunable photonics: Optically active materials and applications from visible to terahertz. iScience *25*, 104727.
56. Kim, G., Kim, D., Ko, S., Han, J.-H., Kim, J., Ko, J.H., Song, Y.M., and Jeong, H.-H. (2024). Programmable directional color dynamics using plasmonics. Microsyst. Nanoeng. *10*, 22.
57. Anulytė, J., Bužavaitė-Vertelienė, E., Stankevičius, E., Vilkevičius, K., and Balevičius, Z. (2022). High spectral sensitivity of strongly coupled hybrid Tamm-plasmonic resonances for biosensing application. Sensors *22*, 9453.
58. Choi, C., Lee, G.J., Chang, S., Song, Y.M., and Kim, D.-H. (2024). Nanomaterial-based artificial vision systems: from bioinspired electronic eyes to in-sensor processing devices. ACS Nano *18*, 1241–1256.
59. Potapova, E., Dremin, V., Zherebtsov, E., Mamoshin, A., and Dunaev, A. (2020). Multimodal optical diagnostic in minimally invasive surgery. Multimodal Optical Diagnostics of Cancer, 397–424.
60. Stanciu, S.G., König, K., Song, Y.M., Wolf, L., Charitidis, C.A., Bianchini, P., and Goetz, M. (2023). Toward next-generation endoscopes integrating biomimetic video systems, nonlinear optical microscopy, and deep learning. Biophy. Rev. *4*, 021307.
61. Shim, M.G., Song, L.M., Marcon, N.E., and Wilson, B.C. (2000). In vivo Near-infrared Raman Spectroscopy: Demonstration of Feasibility During Clinical Gastrointestinal Endoscopy. Photochem. Photobiol. *72*, 146–150.
62. Liu, C., Shi, C., Wang, T., Zhang, H., Jing, L., Jin, X., Xu, J., and Wang, H. (2021). Bio-inspired multimodal 3D endoscope for image-guided and robotic surgery. Opt Express *29*, 145–157.
63. Yang, B., Dong, Y., and Chen, X. (2024). Feature-Enhanced Artificial Visual Perception Based on Superlinear Voltage-Reflectance Responses of Electrochromic Arrays. ACS Photonics *11*, 1909–1919.

64. Chen, X., Hu, D., Mescall, R., You, G., Basov, D.N., Dai, Q., and Liu, M. (2019). Modern scattering-type scanning near-field optical microscopy for advanced material research. Adv. Mater. *31*, 1804774.

65. Fei, Z., Rodin, A.S., Andreev, G.O., Bao, W., McLeod, A.S., Wagner, M., Zhang, L.M., Zhao, Z., Thiemens, M., Dominguez, G., et al. (2012). Gate--tuning of graphene plasmons revealed by infrared nano-imaging. Nature *487*, 82–85.

66. Stanciu, S.G., Tranca, D.E., Pastorino, L., Boi, S., Song, Y.M., Yoo, Y.J., Ishii, S., Hristu, R., Yang, F., Bussetti, G., and Stanciu, G.A. (2020). Characterization of nanomaterials by locally determining their complex permittivity with scattering-type scanning near-field optical microscopy. ACS Appl. Nano Mater. *3*, 1250–1262.

67. Garahan, A., Pilon, L., Yin, J., and Saxena, I. (2007). Effective optical properties of absorbing nanoporous and nanocomposite thin films. J. Appl. Phys. *101*.

68. Ko, J.H., Kim, D.H., Hong, S.H., Kim, S.K., and Song, Y.M. (2023). Polarization-driven thermal emission regulator based on self-aligned GST nanocolumns. iScience *26*, 105780.

69. Kang, J., Yoo, Y.J., Park, J.-H., Ko, J.H., Kim, S., Stanciu, S.G., Stenmark, H.A., Lee, J., Mahmud, A.A., Jeon, H.-G., and Song, Y.M. (2023). DeepGT: Deep learning-based quantification of nanosized bioparticles in bright-field micrographs of Gires-Tournois biosensor. Nano Today *52*, 101968.

70. Ko, J.H., Park, J.H., Yoo, Y.J., Chang, S., Kang, J., Wu, A., Yang, F., Kim, S., Jeon, H.G., and Song, Y.M. (2023). Full-control and switching of optical fano resonance by continuum state engineering. Adv. Sci. *10*, 2304310.

71. Kim, S., Heo, K., Lee, S., Seo, S., Kim, H., Cho, J., Lee, H., Lee, K.-B., and Park, J.-H. (2021). Ferroelectric polymer-based artificial synapse for neuromorphic computing. Nanoscale Horiz. *6*, 139–147.

72. Bu, Y., Xu, T., Geng, S., Fan, S., Li, Q., and Su, J. (2023). Ferroelectrics-electret synergetic organic artificial synapses with single-polarity driven dynamic reconfigurable modulation. Adv. Funct. Mater. *33*, 2213741.

STAR★METHODS

KEY RESOURCES TABLE

REAGENT or RESOURCE	SOURCE	IDENTIFIER
Software and algorithms		
Origin 2022	Origin lab	https://www.originlab.com/
MATLAB R2013b	Mathworks	https://www.mathworks.com/
RSoft	Synopsys	https://www.synopsys.com/
Python 3.10.12	Python Software Foundation	https://www.python.org/
TensorFlow 2.17.0	Google	https://www.tensorflow.org/
NeuroSimV3.0 (Nonlinearity)	Georgia Institute of Technology	https://github.com/neurosim/MLP_NeuroSim_V3.0
Others		
E-beam evaporator	Korea Vacuum Tech	http://www.koreavac.com/index.php
UV-VIS-NIR spectrometer	Jasco Inc.	https://jascoinc.com/
Potentiostat	PalmSens	https://www.palmsens.com/

METHOD DETAILS

Optical simulation

A commercial software (DiffractMOD, RSoft Design Group, USA), utilizing a rigorous coupled-wave analysis (RCWA) method, was employed to calculate the reflectance spectra and the electric field/absorption profiles of active Tamm plasmon. In the optical simulation, the diffraction was considered up to second order and a 0.2 nm grid size was utilized to obtain stable optical efficiency. The complex refractive indices of PEDOT:PSS, obtained from the literature,[25] were employed for accurate spectral results in the optical simulation of NIR range. The effective complex refractive indices of Pr-Si and Au membrane were calculated using commercial MATLAB software (MathWorks, USA) based on the volume averaging theory.[67–70]

Optical characterization and measurement

The reflectance spectra and optical neuromorphic properties of the fabricated samples were analyzed using a UV-VIS-NIR spectrometer (V-770 EX, Jasco Inc., Japan). Additionally, a potentiostat (PalmSens4, PalmSens, Netherlands) was used to perform electrochemical *in situ* doping and dedoping procedures during the measurement process, as illustrated in Figure S15, supplemental information.

Electrochemical setup and measurement

The electrochemical setup consists of a potentiostat (PalmSens4, PalmSens, Netherlands), a reference electrode (silver/silver-chloride, Ag/AgCl), a counter electrode (Pt mesh), and an electrolyte (0.1 mol L^{-1} $TBAPF_6$ in acetonitrile). The electrolyte was prepared by dissolving the tetrabutylammonium hexafluorophosphate (TBAPF-6, Sigma Aldrich) in acetonitrile (anhydrous 99.8%, Sigma Aldrich).

Fabrication of active Tamm plasmon

To fabricate the active Tamm plasmon resonator, a DBR, formed with three pairs of insulators (SiO_2/Si_3N_4), was deposited on a glass substrate using plasma-enhanced chemical vapor deposition (PECVD, System 100, Oxford, USA). The Pr-Si was deposited by electron beam evaporation (KVE-E2000, Korea Vacuum Tech Co., Korea) using the GLAD technique, employing a customized slanted sample holder at a deposition angle of 70°. Additionally, a supporting bar on the slanted sample holder was utilized to control the thickenss variation of the last layer (Pr-Si). Subsequently, Pr-Si was treated with oxygen plasma using a reactive ion etch system (RIE, PLASMA LAB80, Oxford Instruments, UK) to form the hydroxyl groups for the hydrophilic surface. Then, PEDOT:PSS was spin-coated onto the surface of the Pr-Si at 800 rpm for 30 s and dried at 120°C for 15 min to remove the residual solvent. A polytetrafluoroethylene syringe filter with a pore size of 0.45 μm was used to filter the aqueous dispersion of PEDOT:PSS (PH1000, Heraeus Clevios, USA). A porous Au nanomembrane was also deposited using the GLAD technique. Before Au deposition, 3.5 nm of porous Cr layer was deposited as an adhesion layer. The subwavelength scaled nanocolumns exhibit effective medium characteristics, suppressing higher-order diffraction.

Neural network simulation and implementation

The neural network was implemented using Python Software (Python Software Foundation, USA) and TensorFlow API (Google, USA). A total of 5,000 training images and 1,000 test images were selected from the MNIST dataset. Background noise with a noise factor of 30 was added to simulate environmental conditions. The dataset was further preprocessed by applying wavelength-specific reflectance at 1.29 μm, 1.44 μm, and 1.63 μm. Denoising was conducted based on the corresponding reflectance values at each wavelength, and the images were subsequently converted to grayscale to express the reflectance values. The neural network architecture consists of a flattened input layer (28 × 28) and a dense output layer with 10 neurons for digit classification (0–9), using softmax activation. Training was performed with the Adam optimizer (learning rate of 0.0001) for 100 epochs, with a batch size of 32, and sparse categorical cross-entropy as the loss function. Model performance was evaluated using a confusion matrix after the final epoch, and accuracy trends were monitored and analyzed across all epochs.

Porosity modulation based on volume averaging theory (VAT)

The effective refractive index of the material is calculated using volume averaging theory (VAT):[67]

$$n_{eff}^2 = \frac{1}{2}\left(A + \sqrt{A^2 + B^2}\right)$$

$$k_{eff}^2 = \frac{1}{2}\left(-A + \sqrt{A^2 + B^2}\right),$$

where

$$\mathrm{A} = \phi\left(n_d^2 - k_d^2\right) + (1 - \phi)\left(n_c^2 - k_c^2\right), \quad \mathrm{B} = 2n_d k_d \phi + 2n_c k_c (1 - \phi).$$

Here, n_{eff} and k_{eff} is the effective refractive index and effective extinction coefficient. The symbols n_c and n_d denote the refractive indices of the continuous and dispersed phases, respectively. Similarly, k_c and k_d represent the extinction coefficients of both phases. The symbol ϕ corresponds to the porosity.

Weight nonlinearity model

The nonlinearity behavior of the weight update processes is defined as follows:[42]

$$\mathrm{R_{LTP}} = \mathrm{B}\cdot\left(1 - \exp\left(-\frac{\mathrm{P}}{\mathrm{A}}\right)\right) + \mathrm{R_{min}}$$

$$\mathrm{R_{LTD}} = -\mathrm{B}\cdot\left(1 - \exp\left(\mathrm{P} - \frac{\mathrm{P_{max}}}{\mathrm{A}}\right)\right) + \mathrm{R_{max}}$$

$$\mathrm{B} = \frac{(\mathrm{R_{max}} - \mathrm{R_{min}})}{\left(1 - \exp\left(-\frac{\mathrm{P_{max}}}{\mathrm{A}}\right)\right)},$$

where $\mathrm{R_{LTP}}$ and $\mathrm{R_{LTD}}$ denote the reflectance during LTP and LTD processes, respectively. The reflectance changes with number of pulses (P). The experimental values $\mathrm{R_{max}}$ and $\mathrm{R_{min}}$ represent the highest and lowest reflectance. The parameter A controls the nonlinearity, while B is a function of A.

Symmetricity calculation

Symmetricity is defined as the inverse of the symmetric error as follows:[71]

$$\text{Symmetricity} = \frac{1}{\textit{symmetric error}}$$

$$\text{Symmetricity error} = \sum_{k=1}^{k=n} \frac{\left(R_N(k) - R_N(2n-k)\right)^2}{n} = \sum_{k=1}^{k=n} \frac{\left(R(k) - R(2n-k)\right)^2}{n\left(R_{max} - R_{min}\right)^2},$$

where

$$R_N(k) = \frac{R(k) - R_{min}}{R_{max} - R_{min}}.$$

Here, $R(k)$ represents the reflectance at the k^{th} state. Symmetricity representing equivalent changes during both potentiation and depression. R_{min} and R_{max} denote the minimum and maximum reflectance values, respectively, and $R_N(k)$ indicates the normalized reflectance.

Paired-pulsed facilitation equation

The PPF index equation is defined as follows:[72]

$$\text{PPF index} = A_1 \exp\left(-\frac{\Delta t}{\tau_1}\right) + A_2 \exp\left(-\frac{\Delta t}{\tau_2}\right).$$

Here, A_1 and A_2 are the initial facilitation magnitudes, and τ_1 and τ_2 are the relaxation time constants of the two phases, respectively. The symbol Δt represents the pulse interval time.